RSC Advances

PAPER

View Article Online
View Journal | View Issue

Cite this: *RSC Adv.*, 2016, **6**, 83356

Tuning the mechanical properties of cellulose nanofibrils reinforced polyvinyl alcohol composites *via* altering the cellulose polymorphs†

Xiaran Miao,‡[b] Feng Tian,‡[ab] Jinyou Lin,*[ab] Hui Li,[c] Xiuhong Li,[b] Fenggang Bian[b] and Xiangzhi Zhang*[b]

Received 4th June 2016
Accepted 28th August 2016

DOI: 10.1039/c6ra14517e

www.rsc.org/advances

Cellulose nanofibrils (CNF) with polymorphs of cellulose I and II (*i.e.* CNF-I and CNF-II) are different in morphology, aspect ratio, the density of functional groups and mechanical properties, which influence the reinforcement effect for polymer composites. In this work, two kinds of CNFs were fabricated from jute fibers by the TEMPO-mediated oxidation method followed by a mechanical disintegration. Highly transparent polyvinyl alcohol (PVA)/CNF composite films containing varying contents of CNF were obtained *via* evaporating solution blends of PVA and CNF. The mechanical and thermal properties of the PVA/CNF composites were extensively investigated. CNF-I led to a higher Young's modulus of the as-prepared composites than CNF-II did at the same content. The high density of functional groups on the surface of CNF-II enhances the interface interaction between PVA molecular chains and CNF, which result in a better toughness of the resultant composites. Meanwhile, both of CNF-I and CNF-II can improve the thermal stability and lower the degradation rate of PVA. This work provides an insight into the design of CNF reinforced composites with desired properties by altering the polymorphs of CNF.

1. Introduction

Cellulose nanofibrils (CNF), as one kind of cellulose nanomaterials, has recently gained a considerable amount of attention due to their intrinsically appealing properties, such as nanoscale dimensions, high specific surface area, low environmental impact, low density, good mechanical strength, easy functionalization, renewability, and biodegradability.[1] In view of the aforementioned unique properties, the CNFs have shown potential applications in composities as reinforcing agents, pharmaceutics, water treatment area, tissue engineering, catalysts, aerogels, coatings, nanopaper, and wound dressing materials, *etc.*[2–6]

CNF is a nanomaterial containing cellulose fibrils with length in the micrometer and width in the nanometer range, which is substantially composed of both cellulose crystalline regions and amorphous regions.[3,7] The preparation of CNF is initially reported by a mechanical method *via* high shearing followed by a homogenization at high pressure.[8] Subsequently, the preparation method has been developed including multi-pass high-pressure homogenization, enzymatic hydrolysis, direct mechanical fibrillation, 2,2,6,6,-tetramethypipelidine-1-oxyl (TEMPO) mediated oxidation followed by a mechanical disintegration.[9] Presently, the CNF can be generated from these various biological sources, *e.g.*, wood pulp,[10] cotton,[11] tunicate,[12] ramie,[13] jute,[14] bacteria.[15]

Up to now, cellulose is acknowledged to have at least four polymorphs, *i.e.*, cellulose I, II, III and IV.[16] Cellulose I and cellulose II are the polymorphs most investigated.[16,17] It is reported that the intra-sheet bonds in cellulose II lattice are essentially the same as in cellulose I lattice structure, but in addition a variety of inter-sheet hydrogen bonds could form; this imparted stability of cellulose II over cellulose I, explaining why it is possible to convert cellulose I into cellulose II but not in reverse. Due to the difference of these typical structures, the elastic modulus of the crystalline regions of cellulose I and II are different, which have been reported to be 138 and 88 GPa, respectively.[17] This typical result suggested that the CNF with different cellulose polymorphs would also exhibit distinctly different properties, such as mechanical properties and thermal stability.

In recent years, some investigations have dealt with comparisons of the properties of CNF with different cellulose polymorphs, such as CNF-I and CNF-II (*i.e.* CNF with I and II crystalline allomorphs).[18–23] For instance, Wang *et al.*,[20] have

[a]*State Key Laboratory for Modification of Chemical Fibers and Polymer Materials, Donghua University, Shanghai 201620, China. E-mail: jinyoulin82@gmail.com; Fax: +86-21-33931904; Tel: +86-21-33931904*

[b]*Shanghai Synchrotron Radiation Facility, Shanghai Institute of Applied Physics, Chinese Academy of Sciences, Shanghai 201204, China. E-mail: linjinyou@sinap.ac.cn; Zhangxiangzhi@sinap.ac.cn*

[c]*School of Materials Science and Engineering, East China University of Science and Technology, Shanghai 200237, China*

† Electronic supplementary information (ESI) available. See DOI: 10.1039/c6ra14517e

‡ These authors have contributed equally to this work.

prepared the CNF from wood by a mechanical nanofibrillation method, and they showed that the dried sheet of CNF-I has lager tensile strength and Young's modulus than that of CNF-II, but lower fracture strain and less thermal stability. Extensively, Han *et al.*,[19] reported the self-assembling behavior of CNF-I and CNF-II during the process of freeze-drying, and the effect of suspension concentration, particle size, crystal structure, and surface charge were investigated, which laid a foundation for the application of CNF with controllable properties and microstructures.

Nowadays, the incorporation of CNF, using as reinforcing agent, into polymer matrix to alter polymer properties has becoming an attractive topic.[24–26] As expected, the effects of CNF on the structure and properties both of the hydrophilic and hydrophobic polymer composites were well studied.[27–29] These previous works mainly focused on the thermal and mechanical properties of as-prepared composite. For example, Liu *et al.*,[27] reported the preparation of CNF-I reinforced PVA nanocomposite films, and they investigated the effects of CNF-I contents on the chemical or crystalline structure, morphology, thermal and mechanical properties of as-prepared nanocomposite films. Xu *et al.*,[30] compared the reinforcement effect of the CNC and CNF in polymers, and their work showed that the CNF led to higher strength and modulus than did CNC but lower strain-at-failure at the same content. More recently, Martoïa *et al.*,[31] reported an original multi-scale network model that describes the elastic properties of CNF nanocomposites.

However, to the best of our knowledge, few have reported the tuning mechanical properties of CNF reinforced polymer composites *via* altering the cellulose polymorphs, especially, the effect of CNF on polymer crystalline structures and orientation of molecular chain in a dynamic process. In this work, the CNF-I and CNF-II were extracted from jute fibers to reinforce the polymer matrix of PVA. The morphology, surface potential, crystal structure and dispersion stability of as-prepared CNF were examined. The effect of CNF with different polymorphs as reinforcing agent on the crystalline structures, transparency, thermal properties, mechanical properties and orientation of molecular chain in a dynamic process of PVA/CNF composite films were systematically investigated.

2. Experimental section

2.1 Materials

Polyvinyl alcohol (PVA) used in this work was purchased from Sigma-Aldrich with an average molecular weight (M_v) in the range of 85 000 to 124 000. Pristine jute fibers, as a raw material of preparation of CNF (provided by Redbud Textile Tech. Inc., China), were sufficiently dried overnight in a vacuum at 70 °C before use. Sodium hydroxide (NaOH, 97.0%), 2,2,6,6-tetramethylpiperidine-1-oxyl radical (TEMPO, 98%), sodium bromide (NaBr, 99.6%), sodium hypochlorite (NaClO, 12%) and ethanol were purchased from Shanghai Aladdin Chemical Regent Inc., China. All reagents and solvents were used as received without any further purification.

2.2 Preparation of CNF-I and CNF-II

According to our previous work,[21] the pristine jute fibers were cut into powders and dispersed in NaOH solutions with concentrations of 3 wt% and 25 wt%, respectively, at the temperature of 70 °C for 4 h. After being washed with deionized water for several times and dried at 70 °C for 24 h, the alkalized jute fibers (1.0 g) were completely dispersed in deionized water and stirred for 0.5 h, the ratio of material to liquid (w/v) was 1 : 100, then NaBr (0.33 g) and TEMPO (0.033 g) were both completely dissolved in the suspension. The reaction was initiated by adding 12 wt% NaClO solution (20.0 g) and the pH value was adjusted between 10.6 and 10.8 by adding NaOH solution. After stirring for 2.5 h, the ethanol absolute (5 mL) was added to stop the reaction, followed by continuously stirring for several minutes, the final product was washed and the TEMPO-oxidized jute fiber jelly were obtained. Subsequently, the quantified jute fiber jelly was dispersed in 50 mL deionized water followed by a high-speed homogenization (IKA, T18) and the CNF aqueous suspension was prepared. The CNF extracted from the pristine jute fibers with 3 wt% and 25 wt% alkali pretreatment were denoted as CNF-I and CNF-II, respectively.

2.3 Preparation of PVA/CNF composites

The PVA/CNF composite films were prepared by solvent evaporation. PVA was firstly dissolved in deionized water to get an 8 wt% solution. The jute fiber jelly was dispersed in deionized water by a high-speed homogenization with a concentration of 2 wt%. Various amounts of CNF gels were added into PVA solution to make the mixtures comprising 0.5, 1, 5, and 10 wt% of CNF (based on PVA solid weight). The mixed solutions were diluted to a solid content of 5 wt%, then the same quality of the mixed solutions were poured into a mold and dried at room temperature for 48 h. The composite films with different weight fractions of CNF were obtained and designated as PVA/CNF-I-x (x = 0.5, 1, 5, 10) and PVA/CNF-II-x (x = 0.5, 1, 5, 10).

2.4 Characterizations

The morphology of CNF-I and CNF-II was observed by a transmission electron microscope (TEM) (Tecnai G2 F20 S-TWIN) equipped with a Gatan 1k × 1k CCD camera. Optical photographs of the CNF gels were taken by a digital camera (Sony A580L). The morphologies of freeze-dried CNF (0.5 wt% CNF quickly frozen in liquid nitrogen, then freeze-dried at the temperature of −80 °C and the vacuum of 3.5 Pa) were investigated by a field emission scanning electron microscopy (FE-SEM) (S4800, Japan). The Fourier transform infrared (FTIR) spectra of freeze-dried CNF were also measured at a Thermo Nicolet 6700 spectrometer (Thermo Fisher) equipped with the Smart iTR operated on the attenuated total reflectance (ATR) mode in the wave-number range of 4000–630 cm^{-1}. Zeta potential (ξ) of a 0.1 wt% CNF aqueous suspension was measured using a Zetasizer NanoS90 (Malvern Instrument) without adjusting ionic strength.

The UV-vis spectras of the composite films were recorded from 450 to 650 nm^{-1} with a spectrophotometer (UV-1800PC) at

room temperature, the thickness of all the samples was about 180 μm. The dynamic mechanical properties of the composites films were measured using a dynamic mechanical analyzer (DMA Q800, TA Instruments) at a heating rate of 3 °C min^{-1} over the temperature range from −50 to 100 °C. The tensile measurements (QJ-210, Shanghai Qingji Testing Instruments Co., LT., China) were carried out at room temperature with a gauge length of 20 mm and a drawing speed of 0.1 mm s^{-1}, over five specimens were measured for each sample to get an average value. Thermogravimetric analysis (TGA) was carried out with a Netzsch thermal analyzer (TG 209 F3 Tarsus) in the temperature ranging from 50 °C to 700 °C with a heating rate of 10 °C min^{-1} under a nitrogen stream.

The *in situ* small-angle X-ray scattering (SR-SAXS) monitored tensile tests and synchrotron radiation wide-angle X-ray scattering (SR-WAXS) experiments were performed at BL16B1 at Shanghai Synchrotron Radiation Facility (SSRF) ($\lambda = 0.124$ nm, photon flux $\approx 1 \times 10^{11}$, beam size ≤ 0.4 mm $\times$ 0.8 mm). The sample-to-detector distances were 89.5 mm for SR-WAXS (corrected by CeO_2 monocrystal powder) and 1990.2 mm for SR-SAXS (corrected by bull tendon), respectively. In the *in situ* tensile SR-SAXS experiments, the drawing speed was 0.1 mm s^{-1}, data was collected every 15 seconds including acquisition time of 2 seconds.

3. Results and discussion

3.1 Crystalline structure and morphology of as-prepared CNF

It is well-known that the crystalline structure of cellulose can be converted by the process of alkali treatment.[16,21] To confirm the crystalline structure of CNF-I and CNF-II prepared in this work, the FTIR and WAXS were used to characterize these two kinds of samples. The FTIR spectra of CNF-I and CNF-II are shown in Fig. S1,† the characteristic bands of CNF-I at 1602 cm^{-1} assigned to sodium carboxylate groups formed by TEMPO-oxidization, 1409 cm^{-1} assigned to CH_2 symmetric bending, 1159 cm^{-1} corresponding to C–O–C asymmetric stretching at β-glucosidic linkage, 1111 cm^{-1} attributed to ring asymmetric stretching and 899 cm^{-1} ascribed to C–O–C asymmetric stretching at group C_1 were shifted to 1604, 1414, 1157, 1108 and 894 cm^{-1} of CNF-II, respectively, indicating the transition of crystalline structure from cellulose I to cellulose II.[32]

The absorbance bands within 3700–3000 cm^{-1} were sensitive to the changes of intra- and inter-molecular hydrogen bonds related to the transformation from cellulose I to cellulose II.[32] To further investigate the changes of crystalline structure, the band resolutions of the IR spectra (3700–3000 cm^{-1}) are provided in Fig. 1a and b. The same conclusion was achieved that the bands at 3342 cm^{-1} and 3400 cm^{-1} for cellulose I of CNF-I transferred to 3487 cm^{-1} and 3442 cm^{-1} for cellulose II of CNF-II.[33] During the transition of crystal structure, the number of hydrogen bonding sites changes. The IR index (*i.e.*, a ratio of IR intensity at a given wavenumber to that at the reference wavenumber) values were used to analyze the hydroxyl density changes from cellulose I to II, the calculated increased IR index of the –OH stretching vibration with the region 3100 to 3800 cm^{-1} for CNF-II indicated that the CNF-II had more –OH groups on the crystal surface than that of cellulose I.[19,34]

The 1D integrated SR-WAXS curves of freeze-dried CNF-I and CNF-II are shown in Fig. 1c. The Bragg peaks of cellulose I centered at $2\theta = 11.7°$ (101), 13.2° ($10\bar{1}$) and 18.1° (200) in CNF-I

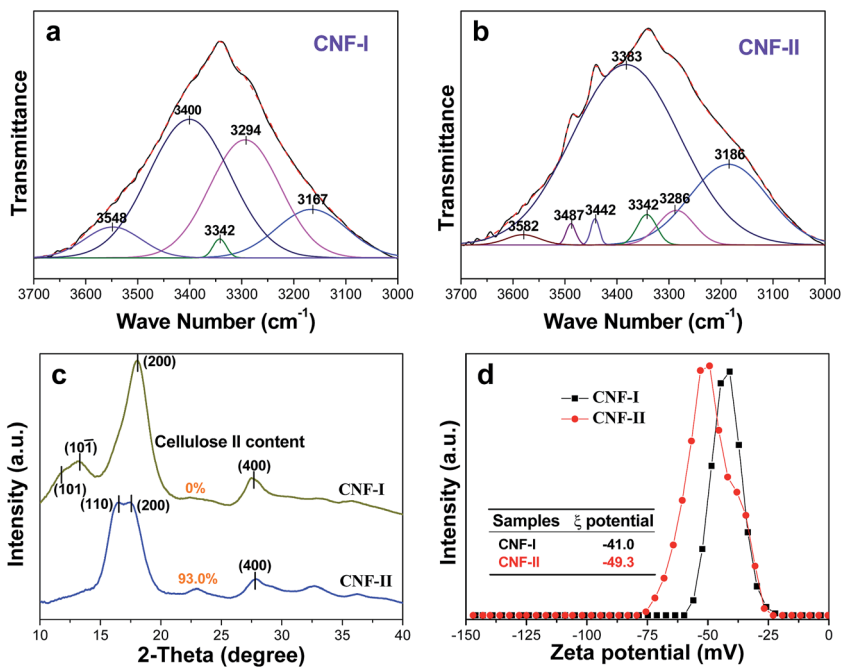

Fig. 1 (a, b) Band resolution of the FTIR spectra of CNF-I and CNF-II. (c) 1D integrated SR-WAXS curves of the freeze-dried CNF-I and CNF-II. (d) Zeta potential of the CNF suspensions.

were converted to cellulose II Bragg peaks located at $2\theta = 16.4^\circ$ (110) and 17.6° (200) in CNF-II.[21,35] In order to obtain the quantitative converted content, the deconvolution was carry out on integrated SR-WAXS curves using 2θ ranging 10 to 22° as shown in Fig. S2.† The cellulose II content was similarly calculated on the basis of the separated area under the peaks of cellulose I and cellulose II.[21,36] The calculated results reveal that the CNF-I is all consist of cellulose I but without any cellulose II, while the CNF-II contains 93.0 wt% cellulose II. It has been concluded that the CNF-I and CNF-II were successfully prepared from alkali pretreated jute fibers with different alkali concentration.

Fig. 1d shows the CNF-I and CNF-II all had narrowly distributed and negative zeta potential (ξ) values of −41.0 and −49.3 mV, respectively. The more highly negative ξ value indicates the more highly converted surface C6 primary hydroxyl to carboxyl that is mostly in the charged sodium salt form. The result suggests the density of carboxyl on the surface of CNF-II is much higher than that of CNF-I.[37]

The morphologies of CNF-I and CNF-II are obviously different as shown in Fig. 2a and b. The CNF-I exhibits rope-like morphology with an average length and diameter of 1120 ± 325 nm and 10 ± 2 nm, respectively. The resultant aspect ratio L/D is ≥110. The slender morphology easily tangles in the aqueous solution to form network and increase resistance to flow, resulting in gel-like behavior of CNF-I even at a very low concentration. The inset of Fig. 2a shows the optical photograph of CNF-I aqueous solution with a concentration of 0.5 wt%, and the viscosity is large enough to resist gravity sedimentation. Due to more amorphous regions of cellulose was dissolved in the alkali pretreatment process with a higher alkali concentration, the CNF-II presents a rod-like morphology with an average length and diameter of 250 ± 30 nm 10 ± 3 nm, respectively, as shown in Fig. 2b, indicating an aspect ratio of ≥25. Thus, the CNF-II displays much lower viscosity than that of CNF-I mainly due to its short length.

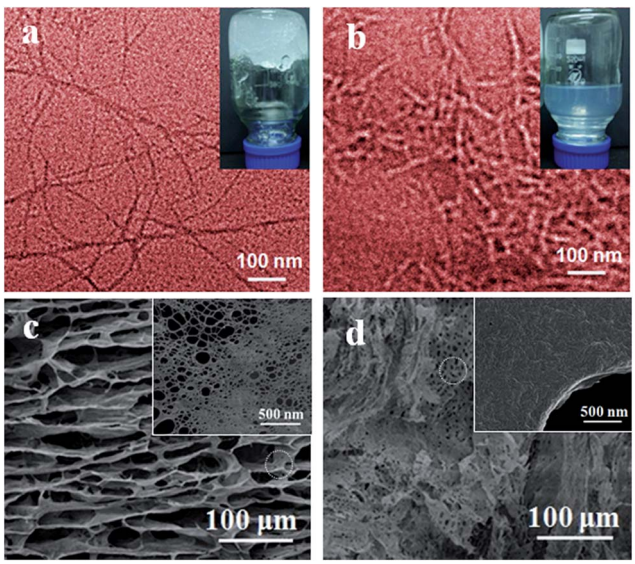

Fig. 2 (a, b) TEM images of CNF-I and CNF-II, the insets of (a) and (b) show the aqueous solution of CNF-I and CNF-II with a concentration of 0.5 wt%, respectively. (c, d) FE-SEM images of freeze-dried CNF-I and CNF-II suspensions.

The morphology of freeze-dried CNF-I and CNF-II suspensions are shown in Fig. 2c and d, respectively. As can be noted, the laminated structure of freeze-dried CNF-I composed of aligned thin layers with an average thickness of 1–3 μm and interval of 20–50 μm was observed. With a high magnification, numerous nanoscale pores with a diameter ranging from dozens to hundreds nanometers are observed in these layers (inset of Fig. 2c). However, the freeze-dried CNF-II exhibits deadwood-like morphology without any lamellar structures at the micrometer scale and the internal pores are beyond nanoscale (inset of Fig. 2d). The result may indicate that the CNF-II pile up more tightly than CNF-I during the process of freeze-drying.

3.2 The effects of crystalline structure and morphology of CNF on crystalline structure of PVA

The incorporation of CNF into polymer matrix may change its crystalline structure. To investigate the effects of crystalline structure and morphology of CNF on crystalline structure of PVA, the SR-WAXS characterization was carried out. Fig. 3 shows 1D integrated SR-WAXS curves of PVA/CNF composites. As can be noted, the 2θ = 18.1° (Fig. 3a) and 2θ = 17.6° (Fig. 3b) scattering peaks representing the (200) lattice plane of cellulose I and cellulose II in the WAXS curves, respectively, the (400) lattice plane of cellulose at $2\theta = 27.6^\circ$ was observed in both PVA/CNF-I and PVA/CNF-II composites, which indicate the existence of CNF-I and CNF-II in these composites. The peaks at 2θ = 15.6°, 16.2°, and 32.5° assigned to $(10\bar{1})$, (101) and (220) lattice planes of PVA, respectively.[38] To further investigate the effect of CNF on the crystal structure of PVA, the band resolutions of SR-WAXS curves are provided in Fig. S3.† The results including full width at half maximum (FWHM), average crystal size in the direction normal to the reflecting plane (B_{hlk}) and the crystalline index of PVA are presented in Table 1. The crystal size was determined by Scherrer equation as following:[30]

$$B_{hlk} = K\lambda/\mathrm{FWHM}\cos\theta \quad (1)$$

where K is the Scherrer constant (0.9 for cellulose)[39] and λ is the X-ray wavelength. The crystalline index of PVA was calculated using the following equation:

$$\mathrm{Cr.I.} = A_{\mathrm{cryst}}/A_{\mathrm{total}*} \quad (2)$$

where A_{cryst} is the sum of crystalline band areas, and $A_{\mathrm{total}*}$ is the total area under the diffractograms except those band areas belong to CNF.

It's interesting to note that there are obvious differences between the influence of CNF-I and CNF-II on the crystal size and crystallinity of PVA in these composite films. In addition to the constant of B_{101} with the addition of CNF, $B_{10\bar{1}}$ increased with the rising of CNF-I contents in PVA/CNF-I composites but a contrary variation was observed in PVA/CNF-II composites. B_{220} remains unchanged with the change of CNF content lower

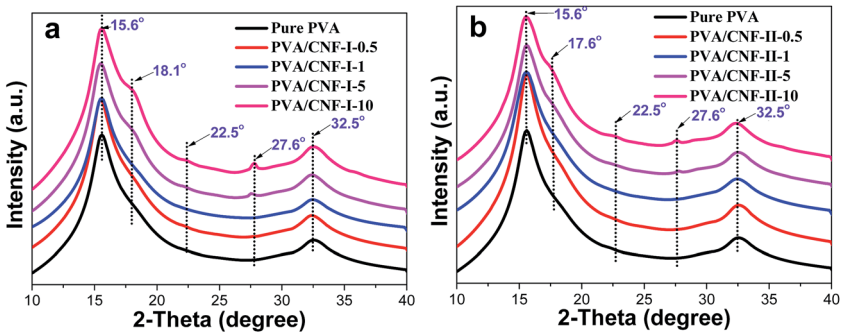

Fig. 3 1D integrated SR-WAXS curves of (a) PVA/CNF-I and (b) PVA/CNF-II composite films with various contents of CNF.

Table 1 SR-WAXS results of pure PVA and PVA/CNF composites

	PVA($10\bar{1}$)			PVA(101)			PVA(220)			Cr.I.
Samples	2θ (°)	FWHM	B (nm)	2θ (°)	FWHM	B (nm)	2θ (°)	FWHM	B (nm)	(%)
Pure PVA	15.6	1.65	3.91	16.4	7.56	0.85	32.7	3.19	2.09	49.9
PVA/CNF-I-0.5	15.5	1.63	3.96	16.4	7.43	0.87	32.5	3.14	2.12	52.9
PVA/CNF-I-1	15.5	1.75	3.69	16.5	8.06	0.80	32.6	2.94	2.27	58.2
PVA/CNF-I-5	15.5	1.52	4.25	16.2	6.71	0.96	32.5	2.16	3.08	68.2
PVA/CNF-I-10	15.5	1.45	4.45	16.3	6.63	0.97	32.7	2.15	3.10	68.7
PVA/CNF-II-0.5	15.6	1.62	3.98	16.4	7.52	0.86	32.7	3.19	2.09	48.7
PVA/CNF-II-1	15.5	1.97	3.28	16.5	7.47	0.86	32.5	3.30	2.02	52.9
PVA/CNCF-II-5	15.6	1.70	3.80	16.0	7.50	0.86	32.7	2.17	3.07	54.5
PVA/CNF-II-10	15.5	1.70	3.80	16.2	6.97	0.93	32.5	2.05	3.25	56.4

than 1 wt% but sharply increases when the content of CNF approaching to 5 wt%. The effect of CNF-I on B_{220} is unobvious in comparison to CNF-II. The crystallinity of PVA increases with CNF-I content and reaches a maximum value of 68.7% at 10 wt% CNF-I, which is more than 12% higher than that of PVA in PVA/CNF-II composites at the same CNF content (56.4% at 10 wt% CNF-II). These discrepancies of PVA crystal structures may be caused by the different morphology and chemical construction between CNF-I and CNF-II such as dimensions and the density of surface functional group. As is known to all, the macro performance of materials is sensitive to the microstructure of themselves, hence, the different crystal size and crystallinity of PVA in PVA/CNF-I and PVA/CNF-II composites will surely lead to the difference of macroscopic properties of these composites.

3.3 The effects of crystalline structure and morphology of CNF on transparency of PVA/CNF composites

Because of the outstanding optical property of pure PVA films,[27] the visible light transmittance (Tr., %) of PVA/CNF composite films mainly depends on CNF size and the dispersion of CNF in PVA matrix. Fig. 4 shows UV-vis light transmittance spectra of PVA/CNF composite films with different CNF contents. The insets display the excellent transparency of all the samples. However, the light transmittances of PVA/CNF-I composite films were lower than PVA/CNF-II composite films at the same CNF content. The Tr. of PVA/CNF-I-0.5 and PVA/CNF-I-1 were 89.47% and 85.34%, respectively, close to that of pure PVA (90.84%). When the CNF content is increased, the Tr. decreases to 57.02% and 54.41% for PVA/CNF-I-5 and PVA/CNF-I-10, respectively. However, the CNF-II almost does not affect the transparency of PVA. The Tr. of PVA/CNF-II composite films only decrease to 88.24% with the increasing of CNF-II content even up to 10 wt%. A possible reason of these distinctions is that the crystallinity of PVA in PVA/CNF-I composite is much higher than that of PVA/CNF-II composite at the CNF content reaching 5 wt%. The excellent transparency of PVA/CNF-II composite films indicates that the CNF-II achieves better dispersion in PVA matrix even at high contents. The excellent optical property of these composites may lead to some potential optical applications.

3.4 The effects of crystalline structure and morphology of CNF on thermal properties of PVA/CNF composites

The effects of CNF on the thermal stability of PVA/CNF composites were examined by using TGA and differential thermal gravity (DTG) shown in Fig. 5. All the samples present two distinct and well-separated turns (200–350 °C and 350–500 °C) in TGA curves (Fig. 5a) and two corresponding weight loss peaks in DTG curves (Fig. 5b). This observation agreed very well with previous publication.[27] Therefore, the thermal degradation of PVA can be roughly regarded as a two-step-degradation. The typical temperatures at 10% weight loss ($T_{-10°C}$) and the maximum weight loss rate (T_p) are employed to evaluate the

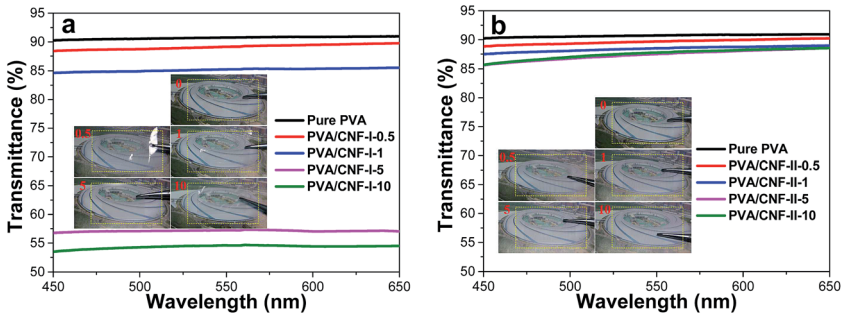

Fig. 4 UV-vis transmittance spectra of (a) PVA/CNF-I and (b) PVA/CNF-II composite films with various contents of CNF. (The insets show the photographs of these composite films.)

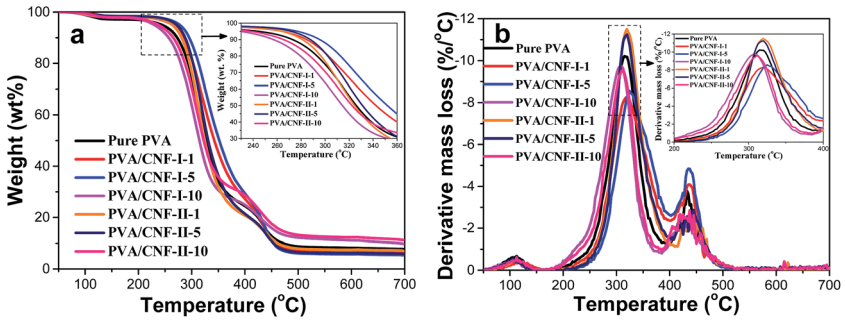

Fig. 5 (a) TGA curves and (b) DTG curves of PVA/CNF composites at a heating rate of 10 °C min^{-1}.

relative thermal stability (see Table S1†). The pure PVA shows a $T_{-10°C}$ of 272.5 °C and T_p of 317.5 °C. Due to the presence of CNF, the TGA/DTG curves of the composites shift to higher temperatures under the CNF contents lower than 5 wt%, the $T_{-10°C}$ of PVA/CNF-I-1, PVA/CNF-I-5, PVA/CNF-II-1 and PVA/CNF-II-5 increases by 12.4, 22.4, 7.4 and 14.9 °C, respectively, and the T_p of PVA/CNF-I-1, PVA/CNF-I-5, PVA/CNF-II-1 and PVA/CNF-II-5 increases by 2.4, 7.4, 1.9 and 2.5 °C, respectively. The increase of $T_{-10°C}$ and T_p demonstrates a better thermal stability of PVA/CNF composites than the pure PVA. Meanwhile, it can be found that the PVA/CNF-I composites are more thermally stable than the PVA/CNF-II composites under a given CNF content, suggesting CNF I enhances the thermal stability and lower the degradation rate of PVA better than CNF II. The result is contradicted with the report by Wang *et al.*,[20] which can be ascribed to the different preparation methods of CNF.

However, when the CNF content is over 5 wt%, the $T_{-10°C}$ and T_p of these composites were decreased and lower than that of the pure PVA. That would be caused by the weight loss of CNF are higher than the pure PVA in the temperature range from 200 to 350 °C. The TGA curves of CNF-I and CNF-II are shown in Fig. S4.† As the increasing of CNF contents, the degradation of CNF can't be overlooked and it will have a large impact on thermal stability of the composites.

3.5 The effects of crystalline structure and morphology of CNF on mechanical properties of PVA/CNF composites

3.5.1 Dynamic mechanical analysis and classic tensile test. The CNF in nanoscale with a large aspect ratio and high mechanical properties makes it become ideal reinforcing agent for polymer matrix. The mechanical reinforcing effects of CNF in PVA were investigated by dynamic mechanical analysis and classic tensile test. The thermo dynamic mechanical property of the PVA/CNF composites is shown in Fig. 6, from which it can be seen that the small content (less than 1 wt%) of CNF has little impact on PVA composites' storage modulus. When the CNF content is up to 5 wt%, a remarkable improvement in the storage moduli is observed, particularly in the temperature range above glass transition temperature (T_g). This significant enhancement may due to the existence of confined network structure induced by CNF in composites.

However, it was observed that the enhancement of CNF-I is stronger than that of CNF-II. For example, the moduli of PVA/CNF-I-5 and PVA/CNF-I-10 are 220% and 1090% higher than that of neat PVA at the temperature of 50 °C, respectively. While the increments are only 160% and 255% for PVA/CNF-II-5 and PVA/CNF-II-10, respectively. The possible reason is that the longer average length and the rope-like morphology of CNF-I are more easily to form continuous 3D network structure in composites, while it is hard for rod-like CNF-II to entangle and form such structure. Therefore, a schematic representation of the dispersions of CNF-I and CNF-II in PVA matrix is proposed as shown in Fig. 7.

The typical stress–strain curves of PVA/CNF composite films are shown in Fig. S5,† the obvious differences in mechanical properties between PVA/CNF-I and PVA/CNF-II composites were observed. Detailed data of Young's modulus, elongation-at-break and yield strength of composites films are shown in

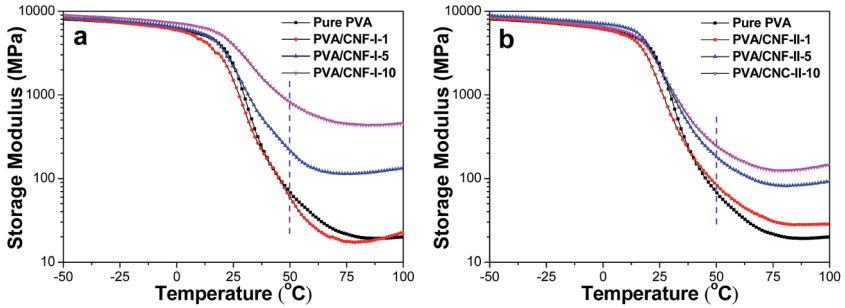

Fig. 6 Storage moduli of (a) PVA/CNF-I and (b) PVA/CNF-II composites as a function of temperature.

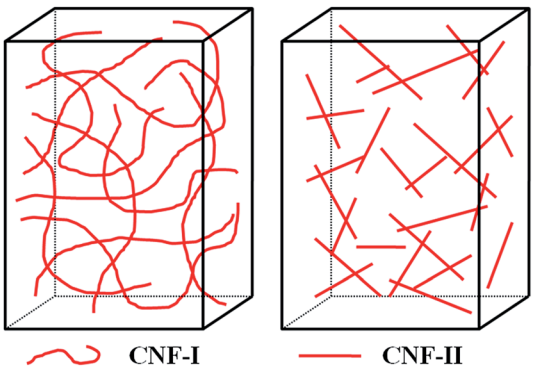

Fig. 7 Schematic representation of the dispersions of CNF-I and CNF-II in PVA matrix.

Fig. 8. It can be seen that the Young's modulus increases from 96.09 MPa for neat PVA to 322.19 MPa for PVA/CNF-I-1 and further to 1473.86 MPa for PVA/CNF-I-10. The elongation-at-break for PVA/CNF-I composites decreases from 320.5% for neat PVA to 89.2% for PVA/CNF-I-10. Notably, although the enhancement of Young's modulus of PVA/CNF-II composites is lower than those of PVA/CNF-I composites (124.93 MPa for PVA/CNF-II-1 and 276.20 MPa for PVA/CNF-II-10), the PVA/CNF-II composites keep a good toughness. As the CNF-II content increased, the elongation-at-breaks of PVA/CNF-II composites are almost unchanged (311.3% for PVA/CNF-II-0.5 and 313.0% for PVA/CNF-II-10). The yield strengths of both PVA/CNF-I and PVA/CNF-II composites increase as the increasing of CNF content. When the composites comprising 10 wt% CNF, the yield strengths are 44.30 MPa of PVA/CNF-I-10 and 44.59 MPa of PVA/CNF-II-10 compared to 39.08 MPa of the neat PVA.

The significant enhancement of rigidity reflecting by the Young's modulus for PVA/CNF-I composites may be attributed to the formation of continuous 3D network structure and the higher crystallinity of PVA in composites induced by CNF-I. However, this 3D network structure will hinder the extension of the composites in the process of drawing. Meanwhile, the interfacial de-bonding between CNF and PVA matrix would occur so that to release strain to PVA matrix, but the relatively high degree of crystallinity will also hinders the extension of PVA molecular chain during the process of stretching.

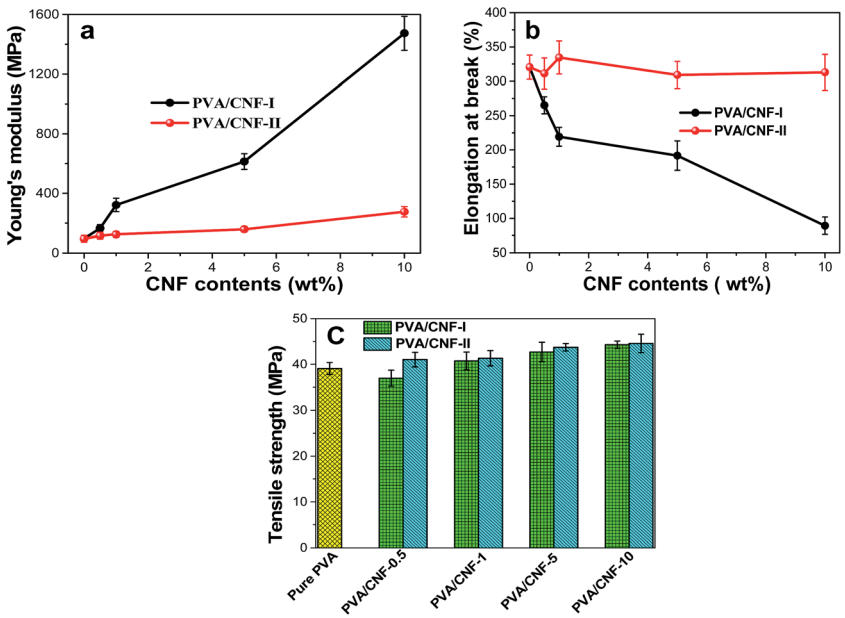

Fig. 8 (a) Young's modulus, (b) elongation-at-break and (c) tensile strength of PVA/CNF composite films as a function of the CNF contents.

Therefore, the microstructure eventually leads to a decline in toughness for PVA/CNF-I composites. CNF-II, with lager density of functional group on the surface, combined more compact with PVA molecular chain, and it's not easy to be separated from PVA matrix when drawing. The rod-like CNF-II is not entangled with each other, and is likely to move with PVA matrix extension. In addition, the crystallinity of PVA in PVA/CNF-II composites was not quite different from that of pure PVA. Thus, the PVA/CNF-II composites can keep the toughness of the pure PVA.

3.5.2 Mechanical property modeling. The Halpin-Tsai model was used to simulate the moduli of the PVA/CNF composites and the results were compared with the experimental results.[40] The model is semi-empirical for short fiber composites and given by the following equation:

$$E_c = \frac{3}{8}E_L + \frac{5}{8}E_T \quad (3)$$

where E_c is the theoretical calculated moduli of the composites. E_L and E_T are the longitudinal and transverse Young's modulus of unidirectional composites, respectively, which were obtained from the following equations:

$$E_L = \frac{1 + 2(l_f/d_f)\eta_L V_f}{1 - \eta_L V_f} E_m \quad (4)$$

$$E_T = \frac{1 + 2\eta_T V_f}{1 - \eta_T V_f} E_m \quad (5)$$

where

$$\eta_L = \frac{(E_{fL}/E_m) - 1}{(E_{fL}/E_m) + 2(l_f/d_f)} \quad (6)$$

$$\eta_T = \frac{(E_{fT}/E_m) - 1}{(E_{fT}/E_m) + 2} \quad (7)$$

where E_m is the measured moduli of the matrix, which was determined from the tensile results. E_{fL} and E_{fT} are the longitudinal and transverse Young's modulus of the filler. l_f and d_f are the length and width of the filler, respectively. For CNF in our study, $E_m = 96.1$ MPa, $E_{fL} = 134$ GPa,[41,42] $E_{fT} = 24.8$ GPa,[41,43] $l_f/d_f = 110$ for CNF-I and $l_f/d_f = 25$ for CNF-II were used. V_f is the volume fraction of filler in the composites and calculated by the densities of CNF-I (1.57 g cm^{-3}), CNF-II (1.54 g cm^{-3})[44] and PVA (1.28 g cm^{-3}).

The experimental moduli of PVA/CNF and the simulation results based on the Halpin-Tsai model are compared against the volume fraction of CNF as shown in Fig. 9. With the change of CNF contents, the Young's moduli of the PVA/CNF-II composites calculated by Halpin-Tsai model were almost consistent with those obtained by experiments. The theoretical Young's moduli of PVA/CNF-I composites calculated by the model were slightly lower than that of the experimental results. These may be caused by the following reasons: (1) the real value of l_f/d_f of CNF-I may be larger than that of we used to in Halpin-Tsai model, (2) the increasing of CNF-I content leads to a large rising in the crystallinity of PVA matrix, which results in the increase of E_m, (3) as the Halpin-Tsai model is based on self-consistent theory by considering a single fiber encased in a cylindrical shell of matrix, the interaction between CNF-I are not considered in this model. In fact, CNF-I can be easily intertwined with each other to form a 3D structure through hydrogen bonds and mechanical interlocking in the PVA matrix, which also contribute to the high moduli of PVA/CNF-I composites. Both experimental and model prediction results show that PVA/CNF-I composite is more rigid than PVA/CNF-II composite, while the elongation-at-break results indicate the PVA/CNF-II composite has better toughness. This result may have a practical significance in developing new polymer/CNF composites with desired comprehensive performance.

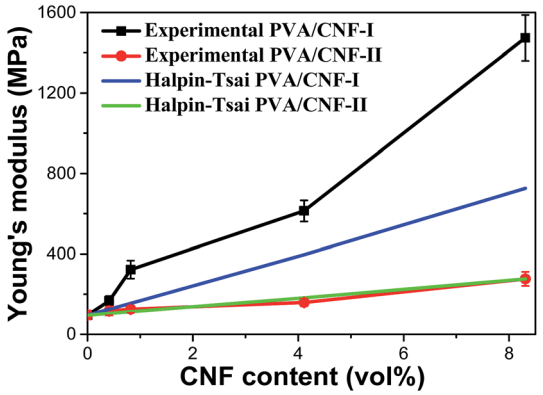

Fig. 9 Experimentally obtained and calculated Young's modulus of PVA/CNF composites as a function of CNF volume fraction.

3.5.3 *In situ* SAXS-mechanical analysis. In order to better understand the reinforcing mechanism of CNF, *in situ* SAXS-mechanical measurement was carried out to investigate the structure evolution of the composites during drawing. Fig. 10 shows 2D SR-SAXS patterns at different stretch time corresponding to the deformation of materials as we carried a uniform speed. The isotropic scatterings are confirmed by the

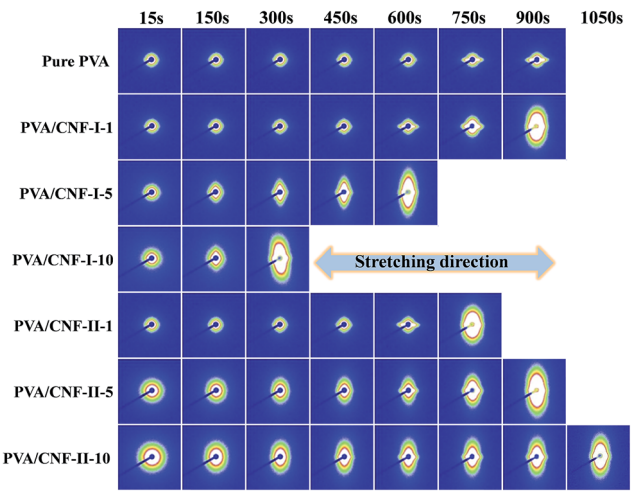

Fig. 10 *In situ* 2D SR-SAXS patterns of PVA/CNF composite films at different stretch time.

SR-SAXS patterns for all samples at the beginning of drawing. When the pure PVA were stretched, the patterns oriented along the tensile direction but almost unchanged perpendicular to the tensile axial. However, PVA/CNF composites oriented in both of the two directions in SAXS patterns. As the CNF contents increased, the orientation along the tensile direction of the PVA/CNF-I composites gradually become weak, and this situation does not present on the PVA/CNF-II composites. However, the orientation perpendicular to the tensile direction of PVA/CNF-I composites, under the same extension length, is more obvious than that of PVA/CNF-II composites at the same CNF content.

The possible mechanism of the structure evolution form according to the SR-SAXS results is schematically proposed and displayed in Fig. 11. During the stretching, the PVA free chain extend along the tensile direction and form regular arrangement, and the PVA crystalline regions and CNF will also orient after the deformation of the composites. The orientation in the vertical direction of the pure PVA does not occur may due to the absence of CNF and a spot of PVA crystalline regions. When a small amount of CNF is added into PVA, only large deformation can lead CNF orientation. With the increasing of CNF contents, the crystallinity of PVA in PVA/CNF-I composites increased significantly according to the WAXS results. Although these increased PVA crystalline regions would hinder the movement of PVA free chain segments to arrange regularly, their own are more likely to be oriented with the extension of the composites. So the orientation along the tensile direction of PVA/CNF-I composites was gradually disappearing as the increasing of CNF contents, and the orientation perpendicular to the tensile direction appeared more and more early. This may be the main reason for PVA/CNF-I composites to become rigidness but easy to break. At the same time, the chain segments of rope-like CNF-I can easily orient than the whole chain of rod-like CNF-II, which also contribute to the early orientation in the vertical direction and the rigidness of PVA/CNF-I composites.

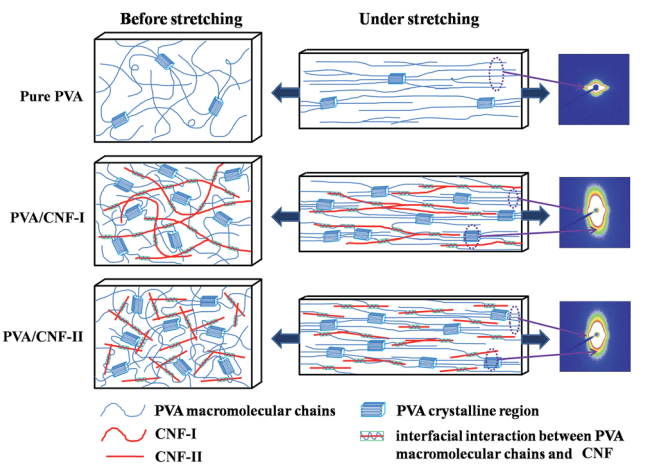

Fig. 11 Schematic presentation of the transformation of microstructure under stretching in pure PVA and PVA/CNF composites. The arrow indicates the stretch direction.

4. Conclusions

In summary, two polymorphs of CNF were isolated from jute fibers by TEMPO-mediated oxidation method followed by a mechanical disintegration. After that the CNF were used to reinforce PVA and the enhanced performances were investigated in detail. All the PVA/CNF composite films displayed a good transparency. CNF-I with a larger aspect ratio may form continuous 3D network structure more easily when compared with CNF-II in PVA matrix and induce more PVA crystalline regions, which can be easily result in the improvement of rigidness for PVA composites. Due to the high density of functional group on the surface of CNF-II, the interface interaction between CNF-II and PVA molecular chains was enhanced, and the presence of CNF-II does not block the movement of PVA free chain segments, thus the PVA/CNF-II composites well retained the toughness of PVA. In addition, both of the two kinds of PVA/CNF composites exhibited an excellent thermal stability, however, the enhancement of PVA thermal stability and lower the degradation rate caused by CNF-I was better than that caused by CNF-II. This work presents an approach to the controllable fabrication of CNF reinforced composite materials with desired properties by altering the cellulose polymorphs.

Acknowledgements

This work is supported by the National Natural Science Foundation of China (No. 51303200, 11505272, U1432115 and 11305254), National Natural Science Foundation for Outstanding Young Scientists (11225527), and State Key Laboratory for Modification of Chemical Fibers and Polymer Materials, Donghua University (LK1481 and LK1503). The beamline BL08U1A of SSRF is appreciated.

References

1 A. W. Carpenter, C. F. de Lannoy and M. R. Wiesner, *Environ. Sci. Technol.*, 2015, **49**, 5277.
2 R. J. Moon, A. Martini, J. Nairn, J. Simonsen and J. Youngblood, *Chem. Soc. Rev.*, 2011, **40**, 3941.
3 A. Isogai, T. Saito and H. Fukuzumi, *Nanoscale*, 2011, **3**, 71.
4 Y. Zhang, T. Nypelö, C. Salas, J. Arboleda, I. C. Hoeger and O. J. Rojas, *J. Renewable Mater.*, 2013, **1**, 195.
5 J. Zhao, X. Zhang, X. He, M. Xiao, W. Zhang and C. Lu, *J. Mater. Chem. A*, 2015, **3**, 14703.
6 R. T. Olsson, M. A. S. A. Samir, G. Salazar-Alvarez, L. Belova, V. Ström, L. A. Berglund, O. Ikkala, J. Nogues and U. W. Gedde, *Nat. Nanotechnol.*, 2010, **5**, 584.
7 J. Zhao, X. He, Y. Wang, W. Zhang, X. Zhang, X. Zhang, Y. Deng and C. Lu, *Carbohydr. Polym.*, 2014, **104**, 143.
8 F. W. Herrick, R. L. Casebier, J. K. Hamilton and K. R. Sandberg, in *Journal of polymer science. Part C, Polymer symposia*, ITT Rayonier Inc., United States, Shelton, WA, 1983.
9 N. Lavoine, I. Desloges, A. Dufresne and J. Bras, *Carbohydr. Polym.*, 2012, **90**, 735.

10 H. Ma, C. Burger, B. S. Hsiao and B. Chu, *Biomacromolecules*, 2011, **12**, 970.
11 C. Spagnol, F. H. A. Rodrigues, A. G. B. Pereira, A. R. Fajardo, A. F. Rubira and E. C. Muniz, *Carbohydr. Polym.*, 2012, **87**, 2038.
12 S. Iwamoto, A. Isogai and T. Iwata, *Biomacromolecules*, 2011, **12**, 831.
13 J. O. Zoppe, M. S. Peresin, Y. Habibi, R. A. Venditti and O. J. Rojas, *ACS Appl. Mater. Interfaces*, 2009, **1**, 1996.
14 J. Lin, L. Yu, F. Tian, N. Zhao, X. Li, F. Bian and J. Wang, *Carbohydr. Polym.*, 2014, **109**, 35.
15 H. W. Liang, Q. F. Guan, L. T. S. Zhu Zhu, H. B. Yao, X. Lei and S. H. Yu, *NPG Asia Mater.*, 2012, **4**, e19.
16 A. O'Sullivan, *Cellulose*, 1997, **4**, 173.
17 T. Nishino, K. Takano and K. Nakamae, *J. Polym. Sci., Part B: Polym. Phys.*, 1995, **33**, 1647.
18 Y. Y. Yue, C. J. Zhou, A. D. French, G. Xia, G. P. Han, Q. W. Wang and Q. L. Wu, *Cellulose*, 2012, **19**, 1173.
19 J. Han, C. Zhou, Y. Wu, F. Liu and Q. Wu, *Biomacromolecules*, 2013, **14**, 1529.
20 H. Wang, D. Li, H. Yano and K. Abe, *Cellulose*, 2014, **21**, 1505.
21 L. Yu, J. Lin, F. Tian, X. Li, F. Bian and J. Wang, *J. Mater. Chem. A*, 2014, **2**, 6402.
22 E. Jin, J. Guo, F. Yang, Y. Zhu, J. Song, Y. Jin and O. J. Rojas, *Carbohydr. Polym.*, 2016, **143**, 327.
23 M. Hirota, N. Tamura, T. Saito and A. Isogai, *Cellulose*, 2012, **19**, 435.
24 J. Yang, C. R. Han, J. F. Duan, M. G. Ma, X. M. Zhang, F. Xu and R. C. Sun, *Cellulose*, 2013, **20**, 227.
25 J. Yang, C. R. Han, X. M. Zhang, F. Xu and R. C. Sun, *Macromolecules*, 2014, **47**, 4077.
26 V. K. Thakur and M. R. Kessler, *Polymer*, 2015, **69**, 369.
27 D. G. Liu, X. Sun, H. F. Tian, S. Maiti and Z. S. Ma, *Cellulose*, 2013, **20**, 2981.
28 R. Endo, T. Saito and A. Isogai, *Polymer*, 2013, **54**, 935.
29 H. Dong, Y. R. Sliozberg, J. F. Snyder, J. Steele, T. L. Chantawansri, J. A. Orlicki, S. D. Walck, R. S. Reiner and A. W. Rudie, *ACS Appl. Mater. Interfaces*, 2015, **7**, 25464.
30 X. Xu, F. Liu, L. Jiang, J. Y. Zhu, D. Haagenson and D. P. Wiesenborn, *ACS Appl. Mater. Interfaces*, 2013, **5**, 2999.
31 F. Martoïa, P. Dumont, L. Orgéas, M. Belgacem and J. L. Putaux, *RSC Adv.*, 2016, **6**, 47258.
32 F. Carrillo, X. Colom, J. Sunol and J. Saurina, *Eur. Polym. J.*, 2004, **40**, 2229.
33 S. Y. Oh, D. I. Yoo, Y. Shin and G. Seo, *Carbohydr. Res.*, 2005, **340**, 417.
34 Y. Yue, C. Zhou, A. D. French, G. Xia, G. Han, Q. Wang and Q. Wu, *Cellulose*, 2012, **19**, 1173.
35 D. Klemm, B. Heublein, H. P. Fink and A. Bohn, *Angew. Chem., Int. Ed. Engl.*, 2005, **44**, 3358.
36 J. G. Slawomir Borysiak, *Fibres Text. East. Eur.*, 2003, **11**, 104.
37 F. Jiang, S. Han and Y. L. Hsieh, *RSC Adv.*, 2013, **3**, 12366.
38 F. A. Rosa Ricciardi, C. De Rosa and F. Lauprêtre, *Macromolecules*, 2004, 1921.
39 F. Xu, Y. C. Shi and D. Wang, *Carbohydr. Polym.*, 2012, **88**, 1149.
40 R. Guzmán de Villoria and A. Miravete, *Acta Mater.*, 2007, **55**, 3025.
41 H. Soeta, S. Fujisawa, T. Saito, L. Berglund and A. Isogai, *ACS Appl. Mater. Interfaces*, 2015, **7**, 11041.
42 K. K. Ichiro Sakurada, K. Nakamae and S. Wadano, *J. Polym. Sci.*, 1962, 10.
43 A. Pakzad, J. Simonsen, P. A. Heiden and R. S. Yassar, *J. Mater. Res.*, 2011, **27**, 528.
44 P. Dhar, D. Tarafder, A. Kumar and V. Katiyar, *RSC Adv.*, 2015, **5**, 60426.